ELSEVIER

International Journal of Heat and Fluid Flow 21 (2000) 213–220

International Journal of
HEAT AND
FLUID FLOW

www.elsevier.com/locate/ijhff

Flow through a rotating helical pipe with circular cross-section

Kyoji Yamamoto *, Md. Mahmud Alam, Junich Yasuhara, Agus Aribowo

Department of Mechanical Engineering, Faculty of Engineering, Okayama University, Okayama 700-8530, Japan

Received 26 March 1999; accepted 14 September 1999

Abstract

The incompressible viscous steady flow through a helical pipe of circular cross-section rotating at a constant angular velocity about the centre of curvature is investigated numerically to examine the combined effects of rotation (Coriolis force), torsion and curvature (centrifugal force) on the flow. It is found that the variation of the total flux with rotation shows a sharp peak when the direction of rotation is negative, that is, in the opposite direction to the pressure-driven flow. The total flux decreases at large rotation. As the torsion increases, the flux first decreases from that of the toroidally curved pipe, reaches a minimum and then increases when the rotation is positive or negative large value. The secondary flow structure in the cross-section of the helical pipe is one cell type when the flux is close to the maximum. There is no bifurcation of the flow.

Keywords: Curved duct flow; Helical pipe flow; Rotating pipe

1. Introduction

The flow through a curved tube has attracted considerable attention not only because of its practical importance in chemical and mechanical engineering, but also because of physically interesting features under the action of centrifugal force caused by curvature of the tube, as is discussed in the review articles by Berger et al. (1983), Nandakumar and Masliyah (1986) and Ito (1987).

The fluid flowing through a tube rotating at a constant angular velocity about an axis normal to a plane including the tube is subject to both Coriolis and centrifugal forces. Such rotating passages are used in cooling systems for conductors of electric generators. Since the tube has more or less a bent or a curved section, it is interesting to investigate the combined effects of curvature and rotation, which are relevant to the flow in rotating curved pipes. Miyazaki (1971) examined the solutions when the pressure-driven flow is in the same direction of rotation. This is called the co-rotating case. Ito and Motai (1974) investigated both co-rotating and counter-rotating cases with respect to the direction of pressure-driven flow. A reduction in the strength of the secondary flow and even a secondary flow reversal was observed for counter-rotating case. Daskopoulos and Lenhoff (1990) discussed the bifurcation characteristics of the flow combined with curvature and rotation. Ishigaki (1996) proposed a formula for the friction factor of the flow in a rotating curved pipe and favourably compared it with the experimental data.

The curved pipe has pitch if it is bent more than one turn. The helical pipe with pitch has been used extensively in various industrial applications to enhance the rate of heat, mass and momentum transfer. In order to improve the performance of these devices, an accurate and reliable analysis of the flow in the helical pipe is necessary. The flow in the helical pipe has been studied for circular (Manlapaz et al. 1980; Wang, 1981; Murata et al., 1981; Germano, 1982; Chen and Fan, 1986; Kao, 1987; Xie, 1990; Tuttle, 1990; Chen and Jan, 1992) and elliptical (Germano, 1989) cross-sections.

The previous theoretical studies of the helical pipe flow mentioned above are limited to small curvature and torsion. Liu and Masliyah (1993) numerically solved the problem of laminar flows in a circular pipe having a non-zero pitch. They discussed in detail secondary flow patterns in a cross-section of the pipe. However, their analysis is limited to small Dean number and small curvature. Yamamoto et al. (1994) investigated numerically the flow through a helical pipe for a wide range of the Dean number, curvature and torsion. They employed the orthogonal coordinate system and solved the equations numerically by applying the spectral method. Yamamoto et al. (1995) also conducted experiments on the flow in helical circular tube over a range of Reynolds numbers from about 500 to 2000. The results reveal rather a large effect of torsion on the flow.

Since there is no study regarding helical pipe with rotation, it is quite useful and interesting to investigate the flow in a rotating helical pipe to understand the flow behaviour.

2. Governing equations

We consider a fully developed flow in a rotating helical circular pipe (see Fig. 1(a)). The helical pipe rotates around the

* Corresponding author. Tel.: +81-86-251-8043; fax: +81-86-251-8266.

E-mail address: yamamoto@fluid.mech.okayama-u.ac.jp (K. Yamamoto).

0142-727X/00/$ - see front matter
PII: S0142-727X(99)00079-X

z-axis with a constant angular velocity Ω_T. Fig. 1(b) shows the coordinate systems used in the present study. Here, s' is the coordinate along the centre-line of the duct, **T** the unit tangent vector along s', and **N** and **B** the normal and binormal vectors, respectively. The right-handed helix is considered in our work. We use the coordinates (r', α, s') proposed by Germano (1982). The angle α is defined by $\alpha = \theta + \phi$, where

$$\phi(s') = \int_{s'_0}^{s'} \tau'(s)\,\mathrm{d}s. \tag{1}$$

Here τ' is the torsion of the centre-line of the pipe and s'_0 is arbitrary as long as $s' \geqslant s'_0$. Variables are non-dimensionalized by using a the radius of the circular tube, v the kinematic viscosity and ρ the density of the fluid. We introduce the non-dimensional variables defined by

$$\begin{aligned} &r = \frac{r'}{a}, \quad u = \frac{a}{v}u', \quad v = \frac{a}{v}v', \quad w = \frac{a}{v}w'\sqrt{2\delta}, \\ &\delta = a\delta', \quad \lambda = a\tau', \quad p = \left(\frac{a}{v}\right)^2 \frac{p'}{\rho}, \quad s = \frac{s'}{a}. \end{aligned} \tag{2}$$

Here, u, v and w are the velocity components in the (r, α, s) directions, respectively, where p is the pressure, δ the non-dimensional curvature, λ the non-dimensional torsion and the variables with prime are the dimensional quantities. It is shown by Germano (1982) that the coordinates (r, θ, s) are orthogonal systems. Then, the Navier–Stokes equations can be put mathematically in the following non-dimensional forms:

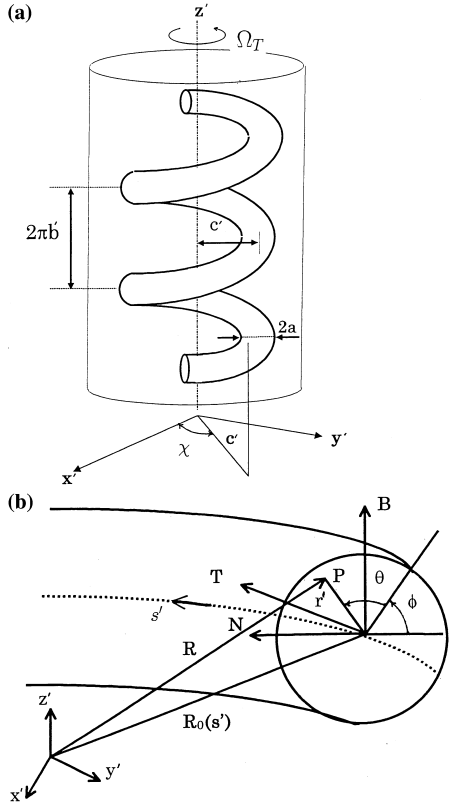

Fig. 1. Coordinate systems: (a) rotating pipe; (b) orthogonal coordinates.

$$\frac{1}{r}\frac{\partial}{\partial r}(ru) + \frac{1}{r}\frac{\partial v}{\partial \alpha} + \frac{\beta_0}{\omega}\frac{\partial w}{\partial \alpha} + \frac{\delta}{\omega}(u\cos\alpha - v\sin\alpha) = 0, \tag{3}$$

$$\begin{aligned} &Du - \frac{v^2}{r} - \frac{\cos\alpha}{\omega}\frac{w^2}{2} + \frac{1}{2}T_r(2\beta_0 v - w\cos\alpha) \\ &\quad = -\frac{\partial p_1}{\partial r} - \left(\frac{1}{r}\frac{\partial}{\partial \alpha} - \frac{\delta\sin\alpha}{\omega}\right)\Omega \\ &\qquad + \frac{\beta_0}{\omega}\frac{\partial}{\partial \alpha}\left(\frac{2\delta\beta_0}{\omega}\frac{\partial u}{\partial \alpha} - \frac{\partial w}{\partial r} - \frac{\delta\cos\alpha}{\omega}w\right), \end{aligned} \tag{4}$$

$$\begin{aligned} &Dv + \frac{uv}{r} + \frac{\sin\alpha}{\omega}\frac{w^2}{2} + \frac{1}{2}T_r(w\sin\alpha - 2\beta_0 u) \\ &\quad = -\frac{1}{r}\frac{\partial p_1}{\partial \alpha} + \left(\frac{\partial}{\partial r} + \frac{\delta\cos\alpha}{\omega}\right)\Omega \\ &\qquad + \frac{\beta_0}{\omega}\frac{\partial}{\partial \alpha}\left(\frac{2\delta\beta_0}{\omega}\frac{\partial v}{\partial \alpha} - \frac{1}{r}\frac{\partial w}{\partial \alpha} + \frac{\delta\sin\alpha}{\omega}w\right), \end{aligned} \tag{5}$$

$$\begin{aligned} &Dw + \frac{\delta\cos\alpha}{\omega}uw - \frac{\delta\sin\alpha}{\omega}vw + T_r\delta(u\cos\alpha - v\sin\alpha) \\ &\quad = \frac{D_n}{\omega} - \frac{2\delta\beta_0}{\omega}\frac{\partial p_1}{\partial \alpha} + \frac{1}{r}\frac{\partial}{\partial r}r\left(\frac{\partial w}{\partial r} + \frac{\delta\cos\alpha}{\omega}w - \frac{2\delta\beta_0}{\omega}\frac{\partial u}{\partial \alpha}\right) \\ &\qquad - \frac{1}{r}\frac{\partial}{\partial \alpha}\left(\frac{2\delta\beta_0}{\omega}\frac{\partial v}{\partial \alpha} - \frac{1}{r}\frac{\partial w}{\partial \alpha} + \frac{\delta\sin\alpha}{\omega}w\right), \end{aligned} \tag{6}$$

where Ω, ω, D and α are defined by

$$\Omega = \frac{\partial v}{\partial r} + \frac{v}{r} - \frac{1}{r}\frac{\partial u}{\partial \alpha}, \quad \omega = 1 + \delta r\cos\alpha,$$

$$D = u\frac{\partial}{\partial r} + \frac{v}{r}\frac{\partial}{\partial \alpha} + \frac{\beta_0}{\omega}w\frac{\partial}{\partial \alpha}, \quad \alpha = \theta + \phi, \quad c = \frac{c'}{a}. \tag{7}$$

The pressure can be written in the form

$$\begin{aligned} p = &-\frac{D_n s}{\sqrt{2\delta}} + p_1(r, \alpha) \\ &+ \frac{T_r^2}{16}(\delta + 2\beta_0^2)[(c + r\cos\alpha)^2 + 2\beta_0^2 c\sin^2\alpha], \end{aligned} \tag{8}$$

where p_1 is the deviation of the pressure in a cross-section, G a constant representing the pressure gradient along the pipe centre-line and c' the distance between the rotating axis and the centre line of the pipe is as shown in Fig. 1(a). The non-dimensional parameters T_r (Taylor number), D_n (Dean number) and β_0 (torsion parameter) are defined as

$$T_r = \frac{2a^2\Omega_T}{v}\sqrt{\frac{2}{\delta + 2\beta_0^2}}, \quad D_n = \frac{Ga^3\sqrt{2\delta}}{\mu v}, \quad \beta_0 = \frac{\lambda}{\sqrt{2\delta}}. \tag{9}$$

Here, Ω_T is the angular velocity of the pipe rotation and μ the viscosity.

Considering the continuity equation (3), we can introduce the pseudo stream function ψ which is related to u, v and w by

$$u = \frac{1}{r\omega}\frac{\partial \psi}{\partial \alpha}, \quad v = -\frac{1}{\omega}\frac{\partial \psi}{\partial r} - \frac{\beta_0 r}{\omega}w. \tag{10}$$

Putting this equation into Eqs. (4)–(6) and eliminating p_1 in the resulting equations, we get the equations for w and ψ. The equations for w and ψ are actually used for numerical computation. These equations are shown in Appendix A.

The boundary conditions at the wall surface are given by

$$w = u = v = 0, \quad \text{or} \quad w = \psi = \frac{\partial \psi}{\partial r} = 0 \quad \text{at} \quad r = 1. \tag{11}$$

3. Flux through the rotating helical pipe

The dimensional mean axial velocity $\bar{w}'$ is expressed by

$$\bar{w}' = \frac{1}{\pi a^2}\int_0^a r'\,\mathrm{d}r'\int_0^{2\pi} w'\,\mathrm{d}\alpha = \frac{\nu}{2a}\frac{k}{\sqrt{\delta}},$$

where

$$k = \frac{\sqrt{2}}{\pi}\int_0^1 r\,\mathrm{d}r\int_0^{2\pi} w\,\mathrm{d}\alpha$$

is the dimensionless flux. We define the non-dimensional mean axial velocity $\bar{w}$ as

$$\bar{w} = \frac{a}{\nu}\bar{w}' = \frac{k}{2\sqrt{\delta}}. \tag{12}$$

The flux of the rotating helical pipe Q_c and that of a straight tube Q_s are given by

$$Q_c = \pi a^2\bar{w}' = \frac{\pi}{2}a\nu\frac{k}{\sqrt{\delta}}, \tag{13}$$

$$Q_s = \frac{\pi G a^4}{8\mu}. \tag{14}$$

Therefore, we have

$$\frac{Q_c}{Q_s} = \frac{4\sqrt{2}k}{D_n}. \tag{15}$$

We define the Reynolds number as

$$R_e = \frac{\bar{w}'(2a)}{\nu} = \frac{k}{\sqrt{\delta}}. \tag{16}$$

4. Method of numerical calculation

The spectral method is applied in the numerical calculation as is used in the previous study (Yamamoto et al., 1994): The Fourier series is used for the circumferential direction α and the series of the Chebyshev polynomial in the radial direction r. That is, we first expand ψ and w as

$$\begin{aligned} w(r,\alpha) &= \sum_{n=1}^{N} w_n^s(r)\sin(n\alpha) + \sum_{n=0}^{N} w_n^c(r)\cos(n\alpha),\\ \psi(r,\alpha) &= \sum_{n=1}^{N} f_n^s(r)\sin(n\alpha) + \sum_{n=0}^{N} f_n^c(r)\cos(n\alpha), \end{aligned} \tag{17}$$

where N is the truncation number of the Fourier series. Substituting the expansions (17) into equations for w and ψ in Appendix A and equating the coefficients of $\sin(n\alpha)$ and $\cos(n\alpha)$ $(n = 0, 1, \ldots)$, we have the nonlinear differential equations for $f_n^s(r)$, $f_n^c(r)$, $w_n^s(r)$ and $w_n^c(r)$. By introducing a new variable $R = 2r - 1$, these equations together with the boundary conditions are written as:

$$\left\{(R+1)^2\frac{\mathrm{d}^2}{\mathrm{d}R^2} + (R+1)\frac{\mathrm{d}}{\mathrm{d}R} - n^2\right\}w_n^s(R) = \frac{(R+1)^2}{4}\{Q_n^s(R) - R_n^s(R)\}, \tag{18}$$

$$\begin{aligned} &w_n^s(1) = 0 \quad (n \geqslant 1),\\ &w_0^s(1) = 0 \quad (n = 1), \end{aligned} \tag{18a}$$

$$\left\{(R+1)^2\frac{\mathrm{d}^2}{\mathrm{d}R^2} + (R+1)\frac{\mathrm{d}}{\mathrm{d}R} - n^2\right\}w_n^c(R) = \frac{(R+1)^2}{4}\{Q_n^c(R) - R_n^c(R)\}, \tag{19}$$

$$\begin{aligned} &w_n^c(1) = 0 \quad (n \geqslant 1),\\ &w_0^c(1) = 0 \quad (n = 1), \end{aligned} \tag{19a}$$

$$\left\{(R+1)^2\frac{\mathrm{d}^2}{\mathrm{d}R^2} + (R+1)\frac{\mathrm{d}}{\mathrm{d}R} - n^2\right\}^2 f_n^s(R) = \frac{(R+1)^2}{16}\{S_n^s(R) - T_n^s(R)\}, \tag{20}$$

$$\begin{aligned} &f_n^s(1) = f_n^{s'}(1) = 0 \quad (n \geqslant 1),\\ &f_0^s(1) = f_0^{s'}(1) = 0 \quad (n = 1), \end{aligned} \tag{20a}$$

$$\left\{(R+1)^2\frac{\mathrm{d}^2}{\mathrm{d}R^2} + (R+1)\frac{\mathrm{d}}{\mathrm{d}R} - n^2\right\}^2 f_n^c(R) = \frac{(R+1)^2}{16}\{S_n^c(R) - T_n^c(R)\}, \tag{21}$$

$$\begin{aligned} &f_n^c(1) = f_n^{c'}(1) = 0 \quad (n \geqslant 1),\\ &f_0^c(1) = f_0^{c'}(1) = 0 \quad (n = 1), \end{aligned} \tag{21a}$$

where the right-hand sides of the above equations have complicated nonlinear forms consisting w_n^s, w_n^c, f_n^s, and f_n^c. We will not show these explicit forms for shortness. Next we expand w_n^s, w_n^c, f_n^s, f_n^c in terms of the Chebyshev polynomials as follows:

$$w_n^s(r) = \sum_{m=0}^{M} W_{nm}^s\Phi_{nm}(R), \quad w_n^c(r) = \sum_{m=0}^{M} W_{nm}^c\Phi_{nm}(R), \tag{22}$$

$$f_n^s(r) = \sum_{m=0}^{M} F_{nm}^s\Psi_{nm}(R), \quad f_n^c(r) = \sum_{m=0}^{M} F_{nm}^c\Psi_{nm}(R), \tag{23}$$

where

$$\begin{aligned} &n \geqslant 1, \quad \Phi_{nm}(R) = (R-1)(R+1)T_m(R),\\ &n = 0, \quad \Phi_{nm}(R) = \begin{cases} (R-1)(R+3) & (m=0),\\ (R-1)(R+1)^2T_m(R) & (m\neq 0),\end{cases}\\ &n \geqslant 2, \quad \Psi_{nm}(R) = (R-1)^2(R+1)^2T_m(R),\\ &n = 1, \quad \Psi_{nm}(R) = \begin{cases} (R-1)^2(R+1)(R+3) & (m=0),\\ (R-1)^2(R+1)^2T_{m-1}(R) & (m\neq 0),\end{cases}\\ &n = 0, \quad \Psi_{nm}(R) = \begin{cases} (R-1)^2(R^2+3R+3) & (m=0),\\ (R-1)^2(R+1)^2T_m(R) & (m\neq 0),\end{cases}\\ &T_m(R) = \cos\{m\cos^{-1}(R)\}. \end{aligned} \tag{24, 25}$$

Here, W_{nm}^s, W_{nm}^c, F_{nm}^s and F_{nm}^c are unknown constants, M is the truncation number of the polynomial series, and $T_m(R)$ is the mth order Chebyshev polynomial. The expansion functions Φ_{nm} and Ψ_{nm} are taken so that ψ and w satisfy the boundary conditions Eq. (11) and the non-singular condition at $r = 0$. We put the expansions (22) and (23) together with the above polynomials into the differential equations (18)–(21a) and use the collocation method to solve these equations. The collocation points are taken as

$$R = \cos\left\{\frac{M+2-i}{M+2}\right\}\pi \quad (1 \leqslant i \leqslant M+1). \tag{26}$$

Then, we have the nonlinear algebraic equations for W_{nm}^s, W_{nm}^c, F_{nm}^s and F_{nm}^c. The algebraic equations are solved by an iteration method with under-relaxation. Convergence of the solution is assured by taking a small value of

$$\epsilon^p = \sum_{n=1}^{N}\sum_{m=0}^{M}\left[(F_{mn}^{s(p)} - F_{mn}^{s(p+1)})^2 + (W_{mn}^{s(p)} - W_{mn}^{s(p+1)})^2\right] + \sum_{n=0}^{N}\sum_{m=0}^{M}\left[(F_{mn}^{c(p)} - F_{mn}^{c(p+1)})^2 + (W_{mn}^{c(p)} - W_{mn}^{c(p+1)})^2\right], \quad (27)$$

where the superscript p denotes the iteration number. Actually, ϵ^p was taken to be less than 10^{-5} in most calculations.

5. Results and discussions

The main flow is forced by the pressure gradient along the centre-line of the pipe. The helical tube is rotated around the centre of curvature of the duct with angular speed Ω_T. According to the definition of T_r, the positive T_r means that the pipe rotates in the same sense as the axial velocity of the fluid within the pipe and we call this as co-rotation. On the other hand, the negative T_r is the case that the helical pipe rotates in the opposite sense with respect to the axial velocity, and this is called the counter-rotation. Numerical calculations have been made of the Dean numbers D_n, 500 and 1000, for two cases of curvature δ, 0.01 and 0.2, and the Taylor numbers T_r ranging from -500 to 500, and of the torsion parameter β_0 covering from 0.0 to 1.2. The truncation number was taken to be $M = 35$ and $N = 60$ with good accuracy. We have the bifurcation of the flow for a toroidal pipe where $\beta_0 = 0.0$ (Daskopoulos and Lenhoff, 1990). However, we did not obtain the bifurcation for a helical pipe where $\beta_0 \neq 0.0$.

5.1. Variation of the flux and the flow behaviours with rotation

First, we describe the variation of the flux and the flow behaviours with rotation for two cases of the Dean number. The curvature δ is taken to be 0.01 and 0.2. The torsion parameter β_0 is kept constant to be 0.4.

Case 1: $D_n = 500$. Fig. 2 shows the flux ratio Q_c/Q_s (where Q_s is the flux through the straight tube and Q_c the flux through the rotating helical pipe at the same pressure gradient G) through the pipe versus the Taylor number T_r at $\delta = 0.01$ and 0.2, and $\beta_0 = 0.4$. The figure indicates that the flux increases as T_r decreases from zero and it has a sharp peak close to the points where $T_r = -140$ for $\delta = 0.01$ and $T_r = -145$ for $\delta = 0.2$, respectively. After that, the flux decreases as T_r further decreases. The flux of $\delta = 0.01$ is larger than that of $\delta = 0.2$. This is well understood if we realise that the pipe with high curvature makes the secondary flow strong and the fluid is not easy to flow. It is interesting to notice that the peaks of the flux for two cases of curvature occur at about the same T_r and that the flux ratios are also about the same and close to unity. There are large differences between the fluxes at large $|T_r|$ in two cases.

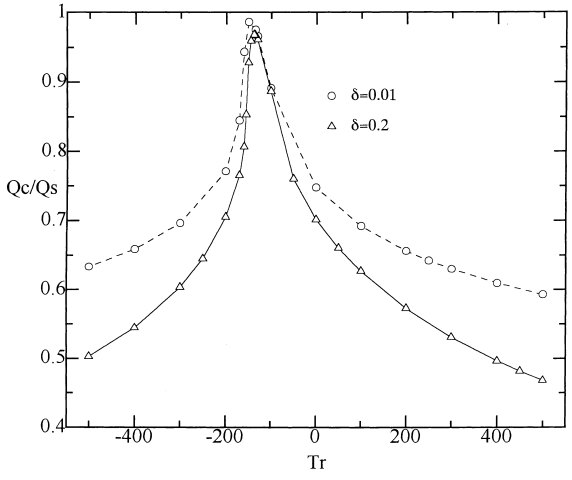

Fig. 2. Flux versus T_r at $D_n = 500$.

We shall depict the flow structures at several points of T_r in Figs. 3(a)–(g) when $\delta = 0.01$. Here and in the following (Fig. 5), the left-hand figures show the vector plots of the secondary flow in a cross-section, while the equi-velocity lines of the axial flow are shown in the right-hand figures. The figures show the view from the upstream of the pipe. The increment of the axial velocity is 10. The outer wall, i.e., $-\mathbf{N}$ direction, is to the right. The length of arrow indicates the ratio of the stream velocity to the mean axial velocity and the direction of the flow in vector plots are always indicated by an arrowhead, no matter how small the flow is. The middle figures show the constant lines of ψ in Eq. (10). The increment of the ψ is 1.0. Tuttle (1990) showed that the iso-ψ lines represent a picture of the secondary flow viewed in the coordinate system (r, θ, s). We have also shown that the constant ψ line is equivalent to the fluid particle trajectory if it is projected on (r, α) plane, although we shall not refer it here for brevity. Therefore, from this figure we can understand the secondary convection of fluid particles in a cross-section of the pipe. The traces of smoke in a visualization photograph taken at a cross-section show the constant ψ lines. On the other hand, the vector plots and the axial velocity contour plots are quantities which are calculated in a cross-section and are measurable experimentally by a pointing device, e.g. a hot-wire anemometer. Therefore, there is a difference in the flow pattern between constant ψ lines and vector plots as is seen in Fig. 3(d). We shall discuss on the variation of the flow behaviour with T_r by using constant ψ lines.

A pair of vortex locates upper left and lower left with unequal size but opposite direction of rotation as shown in Fig. 3(c) at $T_r = 0.0$. The vortex rotating in the counter-direction of torsion (the upper vortex is rotating anti-clockwise) is larger and is at the upper left of the cross-section. On the other hand, the other vortex rotating in the same direction of torsion (lower vortex is rotating clockwise) is a little smaller and is at the lower right of the cross-section (see Fig. 3(c)). This figure also shows the location of the maximum axial velocity being at upper right of the cross-section. Now we decrease T_r to the point where $T_r = -100$. The flow pattern at this point is shown in Fig. 3(d). It will be seen that the previous two vortices become an almost single vortex, which is rotating anti-clockwise. The centre of the vortex moves to the upper left of the cross-section. If further we decrease the value of T_r to the point, where $T_r = -140$ and the flux ratio has almost its peak, the secondary flow shows an interesting feature (see Fig. 3(e)). Only one vortex of the secondary flow is observed and it is more strong near the centre of the cross-section. The velocity near the wall is very weak. The centre of the maximum axial flow is close to the centre of the cross-section. This means that at the peak point the axial flow pattern seems to approach that of the ordinary Poiseuille flow. In this region of the Taylor number, the Coriolis force almost balances with the centrifugal force. If we further increase $|T_r|$ to negative value from the peak point of the flux, then we find that the flux suddenly decreases. That is, the flux has a sharp peak (Fig. 2). The flow pattern after the peak point (where $T_r = -170$) is shown in Fig. 3(f). It is seen from this figure, that one weak vortex, which rotates clockwise, starts to develop near the upper wall of the cross-section. The main vortex occupies most of the area of the cross-section, and these two vortices are reversed type as compared with Fig. 3(c). The maximum axial velocity is shifted to the lower left of the cross-section. Further if we decrease the value of T_r to the point where $T_r = -400$ (see Fig. 3(g)), we get

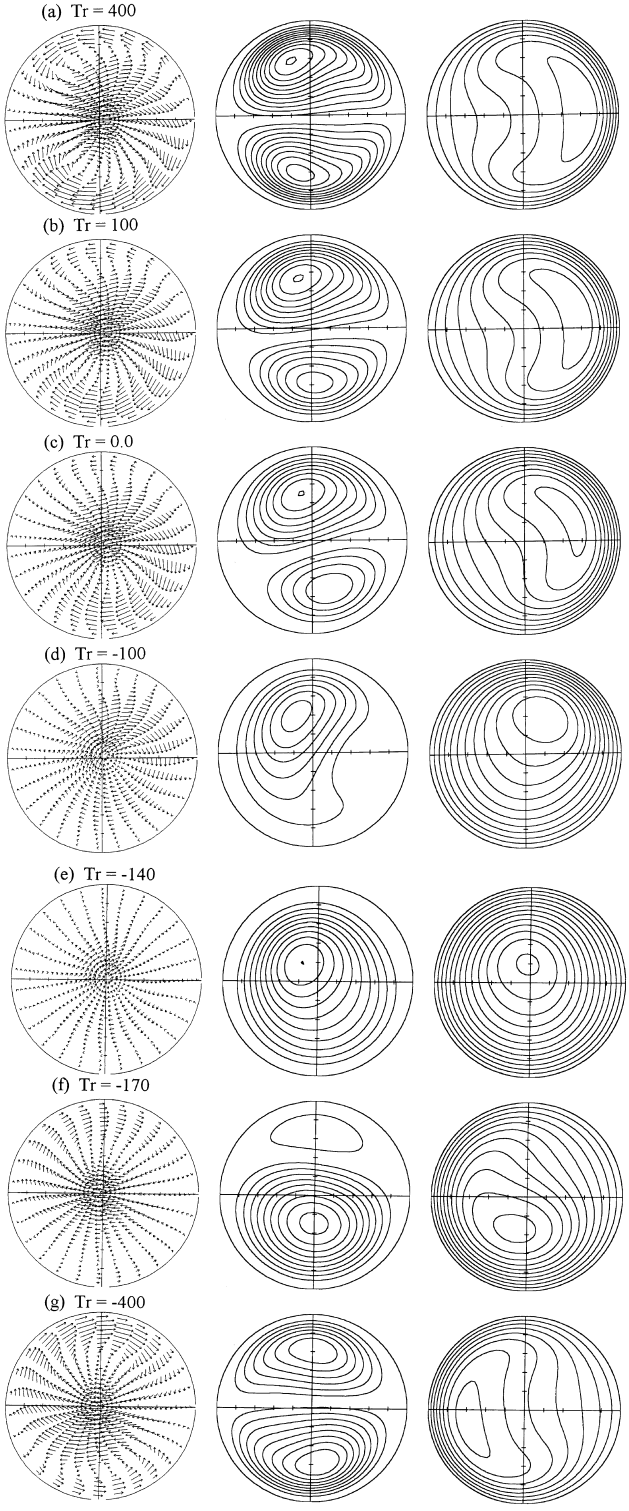

Fig. 3. Flow patterns at $\beta_0 = 0.4$ and $D_n = 500$. The left-hand figure: vector plots of the secondary flow, the middle figure: constant ψ line, the right-hand figure: axial velocity contour.

again two vortices of almost equal size. The flow is completely reversed compared with the flow of $T_r = 0$. The physical mechanism responsible for the reversal of the secondary flow is easily understood once we recognise that the curvature has the tendency to induce a secondary flow directed radially outward in the middle of the channel, while the system rotation has a tendency to induce a secondary flow in radially inward direction. Therefore, the secondary flow is reversed by the action of Coriolis force when T_r has a negative large value. The maximum point of the axial flow (see Fig. 3(g)) approximately shifted to the opposite side as compared to Fig. 3(a) where $T_r = 400$.

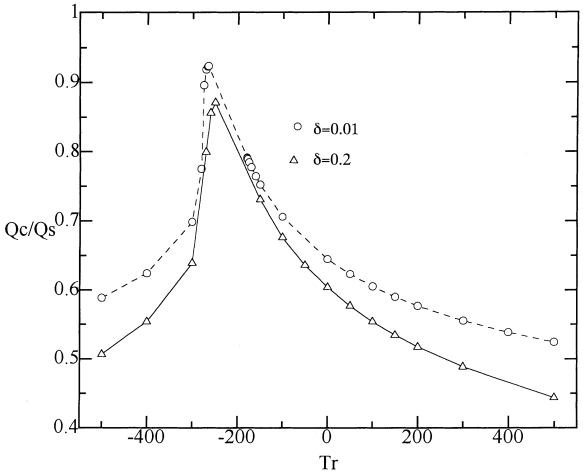

Fig. 4. Flux versus T_r at $\beta_0 = 0.4$ and $D_n = 1000$.

We next proceed to the discussion of the co-rotation. Starting from a point where $T_r = 0$ and increasing T_r, we reach to the point where $T_r = 100$. The flow structure at this point is shown Fig. 3(b). It will be seen that there is no qualitative difference with the flow structure of $T_r = 0$ (Fig. 3(c)). At $T_r = 400$, the secondary flow as well as axial flow behave almost in the same way as in the flow behaviour of $T_r = -400$ but in a reversed way.

Case 2: $D_n = 1000$. Fig. 4 shows the variation of flux ratio with the Taylor number T_r when $D_n = 1000$, $\delta = 0.01$ and 0.2, and $\beta_0 = 0.4$. It will be seen that the flux has a sharp peak at a larger value of $|T_r|$ compared with that of $D_n = 500$. The effect of the centrifugal force is larger at larger D_n. We need large negative Coriolis force, i.e., large T_r, to counterbalance the large centrifugal force. The strong secondary flow caused by the large centrifugal force also makes the fluid difficult to flow. This is responsible for lower value of the flux compared with that of $D_n = 500$. Fig. 5 shows the flow structure. In this figure, the increment of the axial velocity is 20 and the increment of the ψ is 0.5. The constant ψ lines (middle figures) show the fluid particle trajectory in (r, α) plane as is shown in the preceding case. It will be clearly seen from these figures how the variation of the Dean number affects the flow characteristics.

5.2. Variations of the flow with torsion

Fig. 6 shows the variation of the flux ratio with the Taylor number T_r when $D_n = 500$ and $\delta = 0.2$, and when β_0 is taken to be 0.01, 0.4, 0.8 and 1.2. It will be seen from this figure that the flux when $T_r = 0.0$ first decreases with increasing torsion (β_0) and then begins to increase at around $\beta_0 = 0.8$ with further increasing β_0. This is also true for $T_r > 0$ and T_r is less than about -300. However, the variation of the flux with β_0 when $-300 \leqslant T_r \leqslant 0$ is not so simple. For instance, at $T_r = -100$, the flux with large torsion is larger compared with that of small torsion. The flux with large torsion is smaller than that of small torsion at $T_r = -150$.

We depict the flow structure at several points on the curves in Fig. 6 to understand the variation of the flow due to rotation

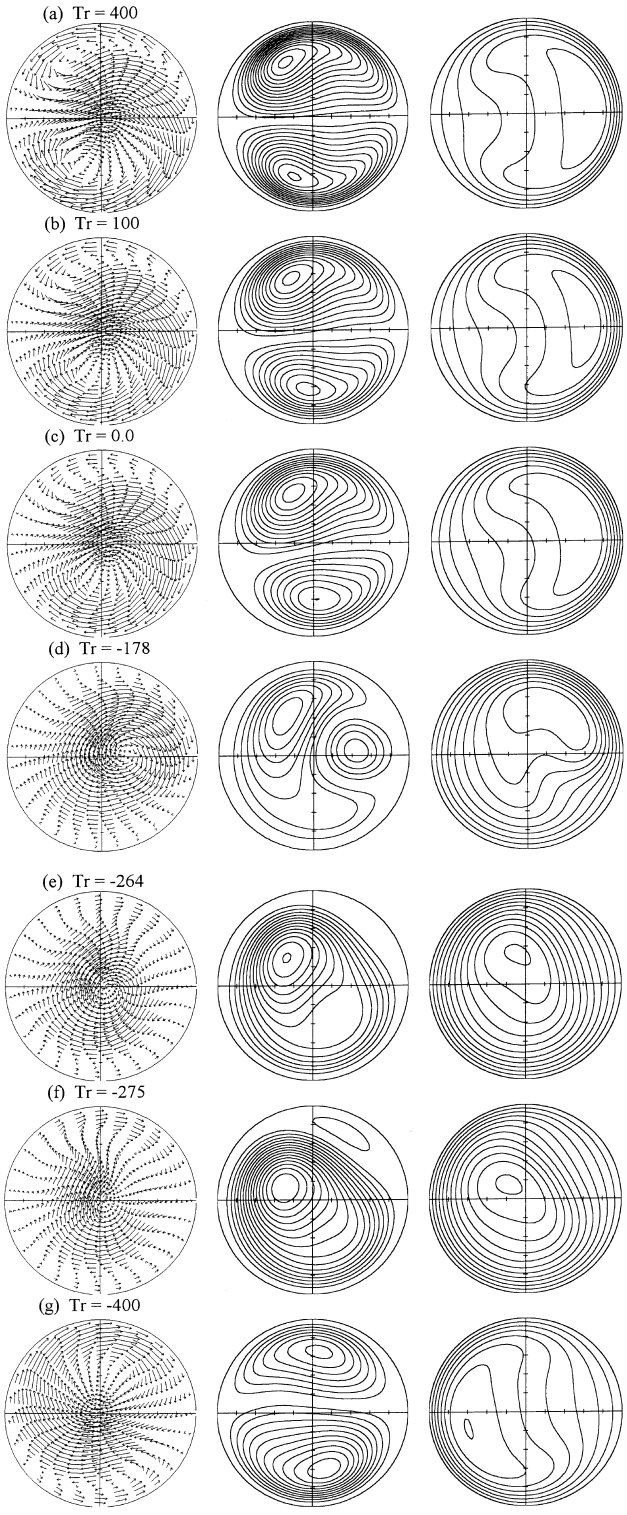

Fig. 5. Flow patterns at $D_n = 500$. The left-hand figure: vector plots of the secondary flow, the middle figure: constant ψ line, the right-hand figure: axial velocity contour.

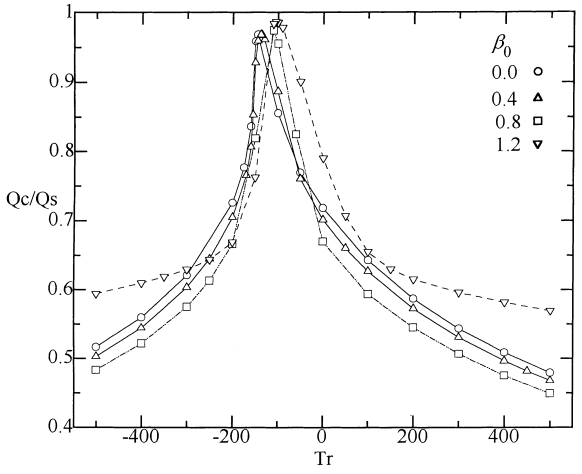

Fig. 6. Flux versus T_r for different values of β_0 .

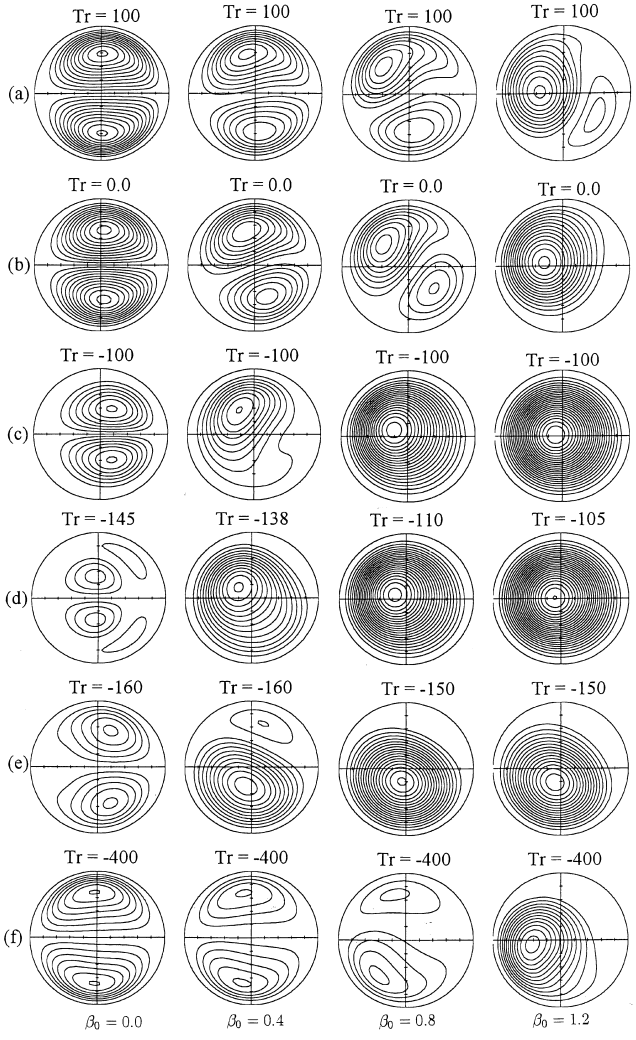

Fig. 7. Variation of the constant ψ lines with T_r and β_0.

as well as torsion. Figs. 7 and 8 show the constant ψ lines of the secondary flow and contour lines of the axial flow velocity for various T_r, respectively. The contour lines of the axial velocity are drawn at every 10 from the tube surface. The increment of ψ is 1.0. When there is no torsion, i.e., $\beta_0 = 0.0$, Daskopoulos and Lenhoff (1990) have made calculations. The Dean numbers of their calculation were different from our Dean number. However, present results without torsion qualitatively agree with their results. The well-known twin

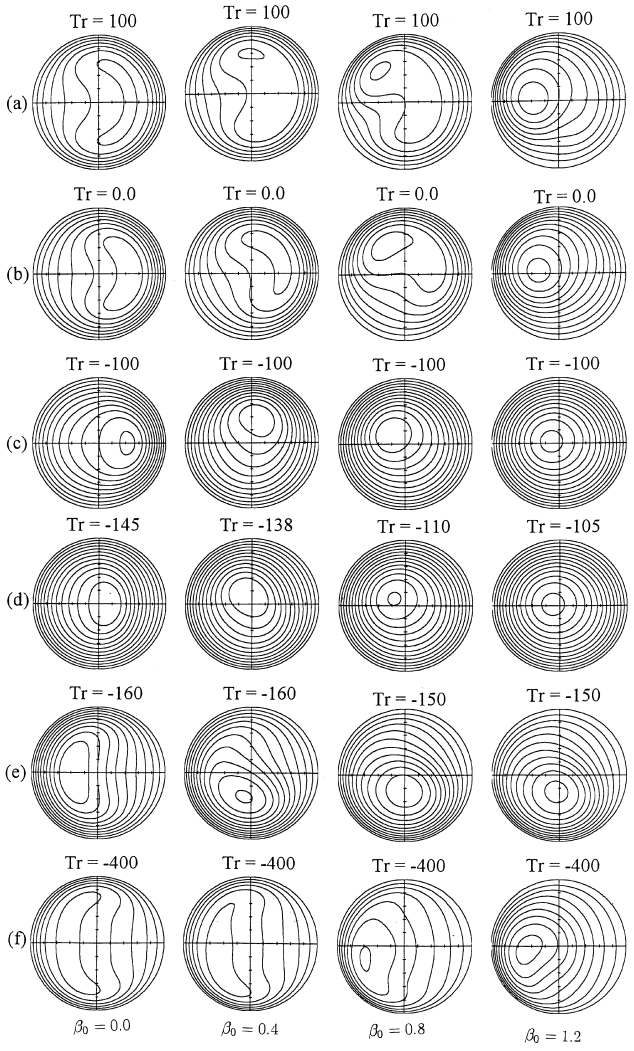

Fig. 8. Variation of the axial velocity contour with T_r and β_0.

vortex without rotation becomes distorted as T_r decreases from zero. There appears second vortex near the wall which rotates in an opposite direction to the original vortex as is shown in Fig. 7(d). The second vortex gradually increases while the first one decreases as decreasing T_r and the second vortex totally occupies the whole region as in Figs. 7(e) and (f). The rotational direction of this vortex is reversed from that of the original one.

We next show the variation of the flow with torsion. When $T_r = 0.0$, the constant ψ lines in Fig. 7(b) show that one of the twin vortex gradually shrinks as β_0 increases and only one vortex occupies the whole cross-section of the pipe. When we take a negative value of T_r, e.g., $T_r = -100$, we see that, in this case too, one of the 2-cell vortex becomes small as β_0 increases and the constant ψ lines show almost concentric circles in the most right-hand figure of Fig. 7(d). If we further decrease T_r, then there appears an additional vortex as is shown in Fig. 7(e). This new vortex has opposite rotational direction to the original one, and increases its strength as T_r further increases (Fig. 7(f)). The secondary flow described by the constant ψ lines shows the one-cell flow rotating anticlockwise at $\beta_0 = 1.2$ if $|T_r|$ is not too large. The axial velocity is almost concentric (see Fig. 8(d)) when the flux is close to a peak in Fig. 6.

Acknowledgements

Authors (Md. Mahmud Alam and Agus Aribowo) would like to express their cordial thanks to the Ministry of Education, Sports and Culture for financial supports.

Appendix A

The equations for w and ψ are given below:

$$\begin{aligned}
\Delta w = {} & \frac{1}{r}\left(\frac{\partial\psi}{\partial\alpha}\frac{\partial w}{\partial r} - \frac{\partial\psi}{\partial r}\frac{\partial w}{\partial\alpha}\right) + \frac{\delta}{\omega}\left(\sin\alpha\frac{\partial\psi}{\partial r} + \frac{\cos\alpha}{r}\frac{\partial\psi}{\partial\alpha}\right)w - D_n \\
& - \delta r(\cos\alpha)\Delta w + \frac{\delta^2}{\omega}w - \delta\Lambda w \\
& + T_r\left[\delta\left(\sin\alpha\frac{\partial\psi}{\partial r} + \frac{\cos\alpha}{r}\frac{\partial\psi}{\partial\alpha}\right) + \frac{2\delta\beta_0^2}{\omega}\frac{\partial\psi}{\partial\alpha}\right] \\
& - \beta_0\left[\frac{2\delta}{\omega}\Omega\frac{\partial\psi}{\partial\alpha} + \frac{2\delta^2\sin\alpha}{r\omega^3}\left\{\left(\frac{\partial\psi}{\partial\alpha}\right)^2 + r^2\left(\frac{\partial\psi}{\partial r}\right)^2\right\}\right. \\
& + \frac{2\delta}{r^2\omega^2}\frac{\partial\psi}{\partial\alpha}\frac{\partial^2\psi}{\partial\alpha^2} + \frac{2\delta}{\omega^2}\frac{\partial\psi}{\partial r}\frac{\partial^2\psi}{\partial\alpha\partial r} \\
& - \left(\frac{2\delta^2\sin\alpha}{r\omega^2} - \frac{3\delta^3\sin 2\alpha}{\omega^3}\right)\frac{\partial\psi}{\partial\alpha} \\
& + \left(\frac{2\delta^2\cos\alpha}{\omega^2} + \frac{6\delta^3 r\sin^2\alpha}{\omega^3}\right)\frac{\partial\psi}{\partial r} \\
& + \frac{4\delta^2\cos\alpha}{r\omega^2}\frac{\partial^2\psi}{\partial\alpha^2} + \frac{4\delta^2\sin\alpha}{\omega^2}\frac{\partial^2\psi}{\partial\alpha\partial r} \\
& \left. - 2\delta r\frac{\partial\Omega}{\partial r} - \frac{2\delta^2 r\cos\alpha}{\omega}\Omega\right] \\
& - \beta_0^2\left[\frac{2\delta^2 r^2\sin\alpha}{\omega^3}w\frac{\partial\psi}{\partial r} + \frac{2\delta r}{\omega^2}\frac{\partial w}{\partial\alpha}\frac{\partial\psi}{\partial r}\right. \\
& \left. + \frac{4\delta^3 r^2\sin^2\alpha}{\omega^3}w + \frac{4\delta^2 r\sin\alpha}{\omega^2}\frac{\partial w}{\partial\alpha} + \frac{4\delta}{\omega}\frac{\partial^2 w}{\partial\alpha^2}\right] \\
& - \beta_0^3\left[\frac{12\delta^4 r^3\sin^2\alpha}{\omega^5}\frac{\partial\psi}{\partial r} + \frac{12\delta^3 r^2\sin\alpha}{\omega^4}\frac{\partial^2\psi}{\partial\alpha\partial r}\right. \\
& \left. + \frac{4\delta^3 r^2\cos\alpha}{\omega^4}\frac{\partial\psi}{\partial r} + \frac{4\delta^2 r}{\omega^3}\frac{\partial^3\psi}{\partial\alpha^2\partial r}\right] \\
& - \beta_0^4\left[\frac{12\delta^4 r^4\sin^2\alpha}{\omega^5}w + \frac{12\delta^3 r^3\sin\alpha}{\omega^4}\frac{\partial w}{\partial\alpha}\right. \\
& \left. + \frac{4\delta^3 r^3\cos\alpha}{\omega^4}w + \frac{4\delta^2 r^2}{\omega^3}\frac{\partial^2 w}{\partial\alpha^2}\right],
\end{aligned}$$

$$\begin{aligned}
\Delta^2\psi = {} & \frac{1}{r}\left(\frac{\partial\psi}{\partial r}\frac{\partial\Omega}{\partial\alpha} - \frac{\partial\psi}{\partial\alpha}\frac{\partial\Omega}{\partial r}\right) + \frac{\delta\Omega}{\omega}\left(\sin\alpha\frac{\partial\psi}{\partial r} + \frac{\cos\alpha}{r}\frac{\partial\psi}{\partial\alpha}\right) \\
& - w\left(\sin\alpha\frac{\partial w}{\partial r} + \frac{\cos\alpha}{r}\frac{\partial w}{\partial\alpha}\right) + \frac{2\delta}{\omega}\Lambda\Delta\psi - \frac{3\delta^2}{\omega^2}\Lambda^2\psi \\
& + \frac{3\delta^3}{\omega^3}\Lambda\psi - T_r\left[\frac{\omega}{2}\left(\sin\alpha\frac{\partial w}{\partial r} + \frac{\cos\alpha}{r}\frac{\partial w}{\partial\alpha}\right)\right. \\
& \left. + \frac{\delta\beta_0}{\omega}\left(\sin\alpha\frac{\partial\psi}{\partial r} + \frac{\cos\alpha}{r}\frac{\partial\psi}{\partial\alpha}\right) + \frac{\delta r\beta_0^2\sin\alpha}{\omega}w + \beta_0^2\frac{\partial w}{\partial\alpha}\right] \\
& - \beta_0\left[-\frac{\delta r\sin\alpha}{\omega}w\Omega - \Omega\frac{\partial w}{\partial\alpha} - \frac{\delta^2\sin^2\alpha}{\omega^3}w\frac{\partial\psi}{\partial\alpha}\right.
\end{aligned}$$

$$
\begin{aligned}
&-\frac{\delta\sin\alpha}{r\omega^2}w\frac{\partial^2\psi}{\partial\alpha^2}+\frac{\delta^2 r\sin 2\alpha}{2\omega^3}w\frac{\partial\psi}{\partial r}+\frac{\delta\cos\alpha}{\omega^2}w\frac{\partial^2\psi}{\partial\alpha\partial r}\\
&-\frac{\delta\sin\alpha}{r\omega^2}\frac{\partial w}{\partial\alpha}\frac{\partial\psi}{\partial\alpha}-\frac{1}{r^2\omega}\frac{\partial w}{\partial\alpha}\frac{\partial^2\psi}{\partial\alpha^2}-\frac{\delta r\sin\alpha}{\omega^2}\frac{\partial w}{\partial r}\frac{\partial\psi}{\partial r}\\
&-\frac{1}{\omega}\frac{\partial w}{\partial r}\frac{\partial^2\psi}{\partial\alpha\partial r}-\frac{\delta}{\omega}\Lambda\frac{\partial}{\partial r}(rw)-\frac{3\delta}{\omega^2}\Lambda w+\frac{\delta^2}{\omega^3}(3w+\omega w)\\
&+\Delta\frac{\partial}{\partial r}(rw)+\frac{1}{\omega}\Delta w+\frac{\delta\sin\alpha}{r\omega^2}\frac{\partial w}{\partial\alpha}-\frac{2\delta\cos\alpha}{r\omega}\frac{\partial^2 w}{\partial\alpha^2}\\
&-\frac{2\delta\sin\alpha}{\omega}\frac{\partial^2 w}{\partial\alpha\partial r}-\frac{\delta(\cos\alpha+\delta r)}{\omega^2}\frac{\partial w}{\partial r}\Big]-\beta_0^2\Big[\frac{\delta^2 r^2\sin 2\alpha}{2\omega^3}w^2\\
&+\frac{\delta r^2 w}{\omega^2}\left(\frac{\cos\alpha}{r}\frac{\partial}{\partial\alpha}-\sin\alpha\frac{\partial}{\partial r}\right)w-\frac{r}{\omega}\frac{\partial w}{\partial\alpha}\frac{\partial w}{\partial r}\\
&+\left\{\frac{9\delta^3\sin 2\alpha}{\omega^4}-\frac{2\delta^2\sin\alpha}{r\omega^3}+\frac{28\delta^4 r\sin^3\alpha}{\omega^5}+\frac{2\delta^4 r\sin\alpha}{\omega^5}\right.\\
&\left.+\frac{\delta^3\sin 2\alpha}{\omega^5}\right\}\frac{\partial\psi}{\partial\alpha}+\left\{\frac{8\delta^2\cos\alpha}{r\omega^4}+\frac{8\delta^3}{\omega^4}+\frac{22\delta^3\sin^2\alpha}{\omega^4}\right\}\frac{\partial^2\psi}{\partial\alpha^2}\\
&+\frac{12\delta^2\sin\alpha}{r\omega^3}\frac{\partial^3\psi}{\partial\alpha^3}+\frac{2\delta}{r^2\omega^2}\frac{\partial^4\psi}{\partial\alpha^4}\\
&+\left\{(22-8\delta r\cos\alpha)\frac{\delta^3 r\sin^2\alpha}{\omega^5}+\frac{4\delta^2\cos\alpha}{\omega^4}-\frac{4\delta^3 r}{\omega^4}\right\}\frac{\partial\psi}{\partial r}\\
&+\left\{\frac{2\delta^2 r\cos\alpha}{\omega^3}+\frac{6\delta^3 r^2\sin^2\alpha}{\omega^4}\right\}\frac{\partial^2\psi}{\partial r^2}+12(1-\delta r\cos\alpha)\\
&\times\frac{\delta^2\sin\alpha}{\omega^4}\frac{\partial^2\psi}{\partial\alpha\partial r}+(1-2\delta r\cos\alpha)\frac{2\delta}{r\omega^3}\frac{\partial^3\psi}{\partial\alpha^2\partial r}\\
&+\frac{6\delta^2 r\sin\alpha}{\omega^3}\frac{\partial^3\psi}{\partial\alpha\partial r^2}+\frac{2\delta}{\omega^2}\frac{\partial^4\psi}{\partial\alpha^2\partial r^2}\Big]-\beta_0^3\Big[\Big\{2(3-\delta r\cos\alpha)\\
&\times\frac{\delta^2 r\cos\alpha}{\omega^4}+6(4-\delta r\cos\alpha)\frac{\delta^3 r^2\sin^2\alpha}{\omega^5}\Big\}w\\
&+6(3-\delta r\cos\alpha)\frac{\delta^2 r\sin\alpha}{\omega^4}\frac{\partial w}{\partial\alpha}+(2-\delta r\cos\alpha)\frac{2\delta}{\omega^3}\frac{\partial^2 w}{\partial\alpha^2}\\
&+\left\{\frac{2\delta^2 r^2\cos\alpha}{\omega^3}+\frac{6\delta^3 r^3\sin^2\alpha}{\omega^4}\right\}\frac{\partial w}{\partial r}+\frac{6\delta^2 r^2\sin\alpha}{\omega^3}\frac{\partial^2 w}{\partial\alpha\partial r}\\
&+\frac{2\delta r}{\omega^2}\frac{\partial^3 w}{\partial\alpha^2\partial r}\Big],
\end{aligned}
$$

where

$$
\Delta=\frac{\partial^2}{\partial r^2}+\frac{1}{r}\frac{\partial}{\partial r}+\frac{1}{r^2}\frac{\partial^2}{\partial\alpha^2},\quad \Lambda=\cos\alpha\frac{\partial}{\partial r}-\frac{\sin\alpha}{r}\frac{\partial}{\partial\alpha},
$$

$$
\Omega=-\frac{1}{\omega}\left\{\Delta\psi-\frac{\delta}{\omega}\Lambda\psi+\beta_0\left(\frac{\partial}{\partial r}(rw)+\frac{1}{\omega}w\right)\right\}.
$$

References

Berger, S.A., Talbot, L., Yao, L.S., 1983. Flow in curved pipes. Ann. Rev. Fluid Mech. 15, 461–512.

Chen, W.H., Fan, C.N., 1986. Finite element analysis of incompressible viscous flow in a helical pipe. Comput. Mech. 1, 281–292.

Chen, W., Jan, R., 1992. The characteristics of Laminar flow in a helical circular pipe. J. Fluid Mech. 244, 241–256.

Daskopoulos, P., Lenhoff, A.M., 1990. Flow in curved ducts: Part 2 Rotating ducts. J. Fluid Mech. 217, 575–593.

Germano, M., 1982. On the effect of torsion on a helical pipe flow. J. Fluid Mech. 125, 1–8.

Germano, M., 1989. The Dean equations extended to a helical pipe flow. J. Fluid Mech. 203, 289–305.

Ishigaki, H., 1996. Laminar flow in rotating curved pipes. J. Fluid Mech. 329, 373–388.

Ito, H., Motai, T., 1974. Secondary flow in rotating curved pipe. The reports of the Institute of high speed Mechanics, Tohoku University, Sendai, Japan, 29(270), 33-57.

Ito, H., 1987. Flow in curved pipes. JSME Int. J. 30 (262), 543–552.

Kao, H.C., 1987. Torsion effect on fully developed flow in a helical pipe. J. Fluid Mech. 184, 335–356.

Liu, S., Masliyah, J.H., 1993. Axially invariant laminar flow in helical pipes with a finite pitch. J. Fluid Mech. 251, 315–353.

Miyazaki, H., 1971. Combined free- and forced-convective heat transfer and fluid flow in rotating curved circular tube. Int. J. Heat Mass Transfer 14, 1295–1309.

Murata, S., Miyake, Y., Inaba, T., Ogawa, H., 1981. Laminar flow in a helically coiled pipe. Bull. JSME 24, 355–362.

Nandakumar, K., Masliyah, J.H., 1986. Swirling flow and heat transfer in coiled and twisted pipes. In: Mujumdar, A.S., Mashelkar, R.A. (Eds.), Advances in Transport Processes. Wiley Eastern, New Delhi, pp. 49–112.

Tuttle, E.R., 1990. Laminar flow in twisted pipes. J. Fluid Mech. 219, 545–570.

Wang, C.Y., 1981. On the low-Reynolds-number flow in a helical pipe. J. Fluid Mech. 108, 185–194.

Xie, D.E., 1990. Torsion effect on secondary flow in a helical pipe. Int. J. Heat and Fluid Flow 11, 114–119.

Yamamoto, K., Yanase, S., Yoshida, T., 1994. Torsion effect on the flow in a helical pipe. Fluid Dyn. Res. 14, 259–273.

Yamamoto, K., Akita, T., Ikeuchi, H., Kita, Y., 1995. Experimental study of the flow in a helical circular tube. Fluid Dyn. Res. 16, 237–249.